

# On the Influence of $\text{Li}_3\text{InCl}_6$ –PEDOT:PSS Hybrids in Solid-State Batteries Prepared via an Aqueous One-Pot Approach

Elina Nazmutdinova,<sup>[a, b]</sup> Carolin Rosenbach,<sup>[a]</sup> Christina Schmidt,<sup>[c]</sup> Sangchai Sarawutankul,<sup>[d]</sup> Kerstin Neuhaus,<sup>[c]</sup> André Gröschel,<sup>[e]</sup> and Nella M. Vargas-Barbosa<sup>\*[f]</sup>

Solid-state batteries (SSBs) utilizing halide solid electrolytes (SE) have garnered attention due to their enhanced stability when paired with oxide-based cathode active materials. However, the dynamic interparticle contact during cycling in SSBs poses challenges to their stability and performance. To mitigate this problem, in this study, we present a one-pot, aqueous synthesis of composites that integrate ion conductivity, electron conductivity, and mechanical stability into a single material. The developed composites consist of a halide SE, lithium indium chloride ( $\text{Li}_3\text{InCl}_6$ ), and a conductive polymer (CP), poly(3,4-ethylendioxythiophene)/poly(styrene sulfonate) (PEDOT:PSS). The successful synthesis was verified using spectroscopic, thermal, scattering, and microscopy methods, with Kelvin Probe

Force Microscopy (KPFM) demonstrating the distribution of PEDOT:PSS at the grain boundaries between  $\text{Li}_3\text{InCl}_6$  particles. Upon incorporating our composite material with lithium nickel manganese cobalt oxide (NMC) cathode active material (CAM) as catholyte, an increase in the partial electronic transport was observed with increasing CP content. A direct correlation between the partial electronic transport of the catholytes and the initial discharge capacities was demonstrated. This study lays the groundwork for the preparation of multi-functional catholytes under more sustainable conditions, without the need for organic solvents, extremely high temperatures, or special environments.

## Introduction

Worldwide decarbonization goals made the electrochemistry research field take a center stage both at the industrial and academic scenes. With an already matured liquid electrolyte-based Li-ion-battery technology, numerous scientists address the safety and performance issues through the development of SSB solutions.<sup>[1]</sup> Hence, SSBs are seen as promising candidates to surpass conventional lithium-ion batteries because they offer advantages in numerous aspects, including both electrochemical and safety performance for various cell-chemistries.<sup>[2–4]</sup> Additionally, the use of SEs enabled the possibility to replace graphite anodes with high-energy-density lithium metal.<sup>[5,6]</sup>

Notwithstanding diverse advantages, various challenges that still hamper the performance of SSBs must be addressed by the scientific community. The electro-mechano-chemical degradation of SSB cathodes is one of them.<sup>[7,8]</sup> The expansion/contraction of the CAM leads to the loss of the interparticle contact between the CAM and SE. This makes a targeted design of the CAM/SE interface of high importance.<sup>[9–13]</sup> Polymer binders are frequently used to mitigate interparticle contact loss and provide additional mechanical stability in battery electrodes.<sup>[14,15]</sup> However, the polymers used are often intrinsic insulators and may hinder the conductivity (both ionic and electronic) throughout the cathode active components. This necessitates the addition of conductive additives (e.g., conductive carbon) which at the same time increases the overall volume of non-active components in the cathode composite.<sup>[16,17]</sup> Additionally, numerous reports suggest that the addition of highly conductive additives (e.g., carbon black, carbon fibers, carbon nanotube) into the SSB cathode compo-

[a] E. Nazmutdinova, C. Rosenbach  
Institute of Inorganic and Analytical Chemistry  
University of Münster  
Correnstrasse 28/30, 48149 Münster, Germany

[b] E. Nazmutdinova  
International Graduate School for Battery Chemistry, Characterization, Analysis, Recycling and Application (BACCARA)  
University of Münster  
Corrensstrasse 40, 48149 Münster, Germany

[c] C. Schmidt, Dr. K. Neuhaus  
Forschungszentrum Jülich GmbH, IEK-12: Helmholtz Institute Münster  
Corrensstrasse 48, 48149 Münster, Germany

[d] Dr. S. Sarawutankul  
Center of Excellence for Energy Storage Technology (CEST)  
Department of Chemical and Biomolecular Engineering, School of Energy Science and Engineering  
Vidyasirimedhi Institute of Science and Technology (VISTEC)  
21210, Rayong, Thailand

[e] Prof. Dr. A. Gröschel  
Polymer Materials for Energy Storage (PES),  
Bavarian Center for Battery Technology (BayBatt) and Bavarian Polymer Institute (BPI)  
University of Bayreuth  
Universitätsstrasse 30, 95447 Bayreuth Germany

[f] Prof. Dr. N. M. Vargas-Barbosa  
Chair of Electrochemistry  
University of Bayreuth and Bavarian Center for Battery Technology (BayBatt),  
Universitätsstrasse 30, 95447 Bayreuth Germany  
E-mail: nellamarievargas@gmail.com

Supporting information for this article is available on the WWW under <https://doi.org/10.1002/batt.202300434>

© 2023 The Authors. *Batteries & Supercaps* published by Wiley-VCH GmbH. This is an open access article under the terms of the Creative Commons Attribution License, which permits use, distribution and reproduction in any medium, provided the original work is properly cited.

site can impede the transport properties due to the formation of new interfaces resulting from the degradation of the SE.<sup>[18–26]</sup>

Therefore, to design a cathode composite system, a so-called catholyte, consisting of CAM, SE, and functional additives, we considered numerous aspects, including both the electrochemical stability of the components and their facile processability. The superionic halides have recently received much attention because they show high electrochemical stability towards high-potential cathode active materials, and they can be synthesized via solution-based approaches.<sup>[21,27–32]</sup> Additionally, the degree of decomposition for halides was reported as much lower than for the sulfides cell with conductive additives, making halide-based systems even more attractive for an in-depth investigation to mitigate the problem mentioned above.<sup>[18,22–26]</sup> Since the majority of the exploited polymer binders used in the halide-based systems necessitated the use of organic solvents, the interest in the development of the processes with the use of other 'greener' solvents is high.<sup>[33,34]</sup> Overall, performed literature screening suggests that the halide-based systems modified with functional additives remain an under-investigated topic, indicating significant opportunities for academic research.<sup>[18–21,33–38]</sup> Furthermore, the point that the targeted interfacial design with the use of functional additives reports to improve the performance of halide-based battery systems was also considered.<sup>[39–41]</sup>

Herein, we propose the use of a functional binder within the cathode composite. Electronically CPs, instead of conventional carbon additives, can help improve interparticle contact, both physical and electronic. Specifically, we can increase the partial electronic conductivity in the cathode composites, which in turn increases the amount of addressed active material without a significant increase in the volume of non-active components. This is expected to boost the transport of electrons during cycling along with an improved initial capacity of the cell (Figure 1). PEDOT:PSS has become the polymer of our choice (see Figure S1 for the chemical structure). PEDOT:PSS, not only being commercially available, shows moderate intrinsic electronic conductivity. This has been reported to be beneficial in improving performance without accelerating the decomposition of the SE.<sup>[20]</sup> Notably, PEDOT:PSS can also be redispersed in water due to the presence of hydrophilic  $-\text{SO}_3\text{H}$

groups in polystyrene sulfonate, PSS, moiety. Thus, we decided to benefit from the advantageous properties of PEDOT:PSS and use it as a component in the composites for SSBs. A direct substitution of the inactive binder and the conductive additive with a single polymer material is expected to result in catholytes that can accommodate volume changes during cycling and provide sufficient electronic conductivity. PEDOT:PSS therefore possesses a dual functionality in our catholyte for SSBs: providing the additional electronic pathways and potentially acting as a binder between the CAM and SE.

Inspired by previous reports on the water-mediated in-situ interfacial growth of  $\text{Li}_3\text{InCl}_6$  on the CAM,<sup>[42]</sup> and the suggested issues on the perturbed electron transport for coated CAM particles,<sup>[43]</sup> we report a water-based synthesis of a composite containing an electronically CP-binder and  $\text{Li}_3\text{InCl}_6$  by in-situ crystallization of  $\text{Li}_3\text{InCl}_6$  in the matrix of redispersed bifunctional CP. The developed synthesis route resulted in high-purity  $\text{Li}_3\text{InCl}_6$  particles covered with CP binder as demonstrated by SEM, EDX, and KPFM measurements. This composite was mixed with an NMC-based CAM and the electrochemical performance of the cathode composites was evaluated via partial electronic conductivity measurements and cycling in SSB half-cells. We observe an increase in the initial discharge capacities of the cells with increasing CP content in the composite materials. Our results set the stage for the processing of catholyte components in a reduced number of steps (one-pot and using water as a green solvent), without compromising the expected performance of the cells.

## Experimental Details

**Materials.** Lithium chloride ( $\text{LiCl}$ , Alfa Aesar, 99%), indium chloride ( $\text{InCl}_3$ , Alfa Aesar, 99.99%), PEDOT:PSS (Sigma Aldrich, redispersible pellets, CP), NMC622 ( $\text{LiNi}_{0.6}\text{Mn}_{0.2}\text{Co}_{0.2}\text{O}_2$ , MSE Supplies, NMC622 polycrystalline), lithium phosphorus sulfur chloride, i.e., sulfide argyrodite ( $\text{Li}_6\text{PS}_5\text{Cl}$ , MSE Supplies, 325 mesh), lithium (Li, 99.9%), indium (In, chemPUR, foil, 100  $\mu\text{m}$  thickness, 99.999%).

**Synthesis of  $\text{Li}_3\text{InCl}_6$ .** The halide solid electrolyte,  $\text{Li}_3\text{InCl}_6$ , was synthesized via a water-mediated process adapted from previously reported procedures.<sup>[29,44,45]</sup> Dried starting materials, namely  $\text{LiCl}$  and  $\text{InCl}_3$  were weighted out and mixed in an Ar-filled glovebox ( $p(\text{O}_2) < 0.1 \text{ ppm}$ ,  $p(\text{H}_2\text{O}) < 0.8 \text{ ppm}$ ) in a 3:1 stoichiometric molar ratio.

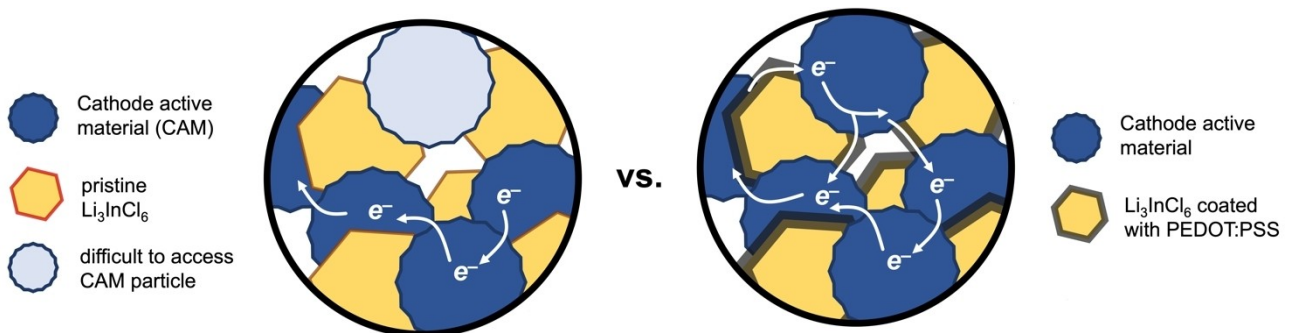


**Figure 1.** Schematic comparison of how the incorporation of PEDOT:PSS, an electronically conducting polymer, will improve the electronic transport as well as the utilization of the cathode active material in solid-state catholytes. In the absence of a conductive additive, cathode active material particles may be more readily isolated from participating in the cycling of the cell.

The mixture of the precursors was dissolved in distilled water (up to 5 mL) in a vial outside of the Ar-filled glovebox. Upon full dissolution of the reagents, water was evaporated at 60 °C for 8 h. A magnetic stirrer was used during the evaporation step for 4 h until  $\text{Li}_3\text{InCl}_6$  crystallization was observed. The hydrated form of  $\text{Li}_3\text{InCl}_6$  ( $\text{Li}_3\text{InCl}_6 \cdot \text{xH}_2\text{O}$ ) was subjected to vacuum drying at 200 °C for an additional 8 h to remove the residual water. The as-synthesized  $\text{Li}_3\text{InCl}_6$  (white powder) was transferred into the Ar-filled glovebox and hand-ground for 15 min in an agate mortar before further use.

**Synthesis of  $\text{Li}_3\text{InCl}_6$  | CP composites.** Dry  $\text{LiCl}$  and  $\text{InCl}_3$  were weighed in a 3:1 molar ratio, along with different amounts of dried PEDOT:PSS in an Ar-filled glovebox. The weighed amount of CP was chosen to correspond to a final 1, 2, or 5 wt% of CP with respect to the expected  $\text{Li}_3\text{InCl}_6$ . The mixture of  $\text{Li}_3\text{InCl}_6$  precursors as well as the CP were dissolved in distilled water in separate vials and mixed until fully dissolved. Upon dissolution of the components, the aqueous solution of  $\text{Li}_3\text{InCl}_6$  precursors was transferred into the vial of the redispersed CP and thoroughly mixed. Subsequently, water was removed at 80 °C for 12 h without additional mixing during water evaporation. The composite was obtained in a form of dry light gray powder and transferred to a vacuum oven at 200 °C for two dehydration steps (each 4 h). The synthesized composite was hand-ground for 15 min in the agate mortar in between and after the vacuum drying steps inside the Ar-filled glovebox. The obtained product, namely  $\text{Li}_3\text{InCl}_6$  | CPX with X = 1, 2, 5% corresponding to wt% of added CP, was used for characterization and as component of the catholyte in sulfide half-cells.

**Preparation of the catholytes.** For preparing 4 different catholytes, the NMC622 CAM was introduced separately into  $\text{Li}_3\text{InCl}_6$ ,  $\text{Li}_3\text{InCl}_6$  | CP1%,  $\text{Li}_3\text{InCl}_6$  | CP2%, and  $\text{Li}_3\text{InCl}_6$  | CP5% at a ratio of 70:30 wt% and hand ground for 30 min in an agate mortar. Thus, the following cathode composite types were obtained: NMC622 |  $\text{Li}_3\text{InCl}_6$  and NMC622 |  $\text{Li}_3\text{InCl}_6$  | CPX (with X = 1, 2, 5%).

**Powder X-ray Diffraction (PXRD).** The phase purity of the  $\text{Li}_3\text{InCl}_6$  in SE and composite samples was evaluated by PXRD in a Stoe STADI P diffractometer (Debye-Scherrer geometry, Dectris MYTHEN 1 K detector). Cu  $\text{K}\alpha$  radiation ( $\lambda = 1.54 \text{ \AA}$ ) with Ge 111 monochromator was used to acquire spectra within a  $\theta$  range of 10–70°. The powder samples were measured in airtight glass capillaries. The scans were recorded with steps of 3° and a step time of 120 s.

**Thermal analysis (TA).** TGA Q5000IR (TA Instruments) was used to carry out the thermogravimetric analysis (TGA). A standard procedure comprised heating the samples ( $\text{Li}_3\text{InCl}_6$ , CP, and  $\text{Li}_3\text{InCl}_6$  | CPX) with a rate of 10 K/min in the range of 30 °C–900 °C in an alumina pan, supported by a high-temperature platinum pan under nitrogen gas flow of 25 mL/min. It should be noted that the samples were exposed to air for a short time when the samples were transferred into the open alumina crucibles straight from the Ar-filled air-tight transfer module until the samples were placed in the system of the TGA instrument under nitrogen gas flow. To minimize the exposure to the humidity from the air, the Al pans of selected samples were crimped inside of the glovebox in aluminum pans. Subsequently, the air-tight pans were pinned with a needle directly before the TGA measurement, performed in the temperature range of 30 °C–600 °C under nitrogen gas flow (25 mL/min). For analyzing the stability of as-received CP in the presence of oxygen, a TGA measurement was performed in the temperature range of 30 °C–1000 °C under oxygen gas flow (25 mL/min). The treatment of the TGA results was complemented by derivative thermogravimetry (DTG) which shows the derived weight changes upon heating plotted against temperature.

Differential scanning calorimetry (DSC) measurements were performed in aluminum pans (sealed hermetically in dry room

conditions) using a DSC Q2000 (TA Instruments) with a heating rate of 10 K/min in a temperature range between 0 °C–250 °C. The samples were subjected to 3 temperature regimes: heating/cooling cycle followed by the second heating.

**SEM and EDX.** SEM equipped with an Auriga CrossBeam working station from Carl-Zeiss with a field emission gun (Schottky-type) under an acceleration voltage of 3 kV was used to investigate the morphology of the synthesized  $\text{Li}_3\text{InCl}_6$  and composites as powders and in pelletized form. Imaging was performed with an InLens secondary electron detector. The powder samples were dispersed and pressed pellets were placed onto carbon tape attached to SEM stubs and further sputtered with Pt (sputtering layer thickness 10 nm) inside the Ar-filled glovebox. Transfer of the samples from the glovebox was handled in an in-house-designed SEM vacuum sample holder minimizing exposure to air. To study the elemental composition of the samples, EDX with X-Max 80 mm<sup>2</sup> detector under 15 kV of acceleration voltage was used. The acquired data was evaluated with the INCA software (version 5.05, Oxford Instruments).

**Raman Spectroscopy.** Sample preparation for Raman characterization included placing each sample on a microscopy glass slide and sealing it with Kapton® tape inside the glovebox. A Bruker Senterra Raman microscope (laser: 532 nm, 2.5 mW) was used for the measurements. The spectra (resolution 3–5 cm<sup>-1</sup>) were acquired in the range of 100–1700 cm<sup>-1</sup> of Raman shift. Coaddition and integration time varied to obtain resolvable spectra: from 5–10 s for integration time and 10–15 coadditions. The obtained results were treated using the OPUS 7.5 software.

**KPFM.** KPFM measurements were performed with a Cypher ES atomic force microscopy (AFM) system (Oxford Instruments) using ASYELEC-01-R2 tips with a Ti/Ir coating. These tips enable measuring topography parameters and the local surface potential (contact potential difference between Ti/Ir and sample) with a high lateral resolution. The samples were measured in Ar at a constant sample temperature of 32 °C. Measurements were performed in a dual-pass mode: in the first step, the sample topography and changes in the amplitude and phase of the AFM cantilever (which is vibrating at its resonance frequency in free Ar-atmosphere) are recorded. In the second step, the tip is moved to a certain height above the surface and the surface potential (also known as the Volta potential) is measured.<sup>[46]</sup> In addition, information about the local elasticity and adhesion forces can be derived from the variation of the phase signal of the cantilever vibration in interaction with the sample surface. An increase in elasticity and/or local adhesion forces lead to an increased phase signal in this region. Grain size analysis from the topography images was done with the software MountainsSPIP Starter 8.0 by Digital Surf (France).

**Electrochemical characterization.** All measurements were performed in press cells based on a previously reported design that includes a cylindric polyether ether ketone (PEEK) inlet (10 mm diameter) confined between two stainless-steel current collectors.<sup>[47]</sup> The assembly of the cells was done inside an Ar-filled glovebox.

Ionic conductivities of as-synthesized  $\text{Li}_3\text{InCl}_6$  were determined with alternating current (AC) impedance spectroscopy on a VMP-300 potentiostat (BioLogic) in the temperature range of 233–333 K (−40–60 °C). The press cells were filled with 250 mg of  $\text{Li}_3\text{InCl}_6$ . The samples were scanned in the frequency range of 100 mHz–7 MHz with 10 mV of applied sinus amplitude at open circuit potential. The analysis of the recorded spectra was performed in RelaxIS 3 software (rhd Instruments).

Partial electronic conductivities of the cathode components and the composites were determined via direct current (DC) polarization measurements in symmetric cells with ion-blocking, i.e.,

stainless steel (SS) electrodes. A set of different potentials (5 mV, -10 mV, 20 mV, 30 mV) were applied to the symmetric cells at 25°C. The sample mass was ca. 50 mg. For both the ionic conductivity and partial electronic conductivity measurements, the sample was loaded in the PEEK inlet of the press cell and subsequently uniaxially pressed with an applied pressure of 3 t for 3 minutes with a slow pressure release. Partial ionic conductivities of the cathode composites were determined via DC polarization measurements in symmetric cells with electron-blocking set-up, of the following configuration: SS | In/InLi | Li<sub>6</sub>PS<sub>5</sub>Cl | Cathode composite | Li<sub>6</sub>PS<sub>5</sub>Cl | In/InLi | SS. A set of different potentials (3.0 mV, 3.5 mV, 4.0 mV, 4.5 mV, 5.0 mV) were applied to the symmetric cells at 25°C. For the cell assembly, firstly the 80 mg of Li<sub>6</sub>PS<sub>5</sub>Cl was loaded in the PEEK inlet and hand-pressed, further 100 mg of cathode composite was evenly spread on top of the Li<sub>6</sub>PS<sub>5</sub>Cl layer and hand-pressed, followed by a second layer of 80 mg Li<sub>6</sub>PS<sub>5</sub>Cl layer. Further the pellet stack underwent uniaxial pressing at 3 t for 3 minutes. In/InLi was prepared by punching out foils from hand-pressed Li (obtained film of 200 µm thickness, 6 mm diameter) and commercial In foil (9 mm diameter). The metal foils were stacked together to form a stable alloy and placed with In metal adjacent to both sides of argyrodite pellets and with Li to the stainless steel electrode.<sup>[48]</sup>

The sulfide half-cells for galvanostatic charge-discharge studies were assembled in multiple steps. In the first step, 60 mg of Li<sub>6</sub>PS<sub>5</sub>Cl and 50 mg of pristine Li<sub>3</sub>InCl<sub>6</sub> were pressed as a bilayer pellet at 2 t for 1 minutes. Then, 12 mg of the cathode composite (preparation described in the section synthesis of Li<sub>3</sub>InCl<sub>6</sub>|CP composites) was loaded on top of the Li<sub>3</sub>InCl<sub>6</sub>-side of the bilayer SE pellet, evenly spread, and pressed at 3 t for 3 minutes. This amount of cathode composite corresponds to 10.7 mg/cm<sup>2</sup> aerial loading and an aerial theoretical capacity of 2.14 mAh/cm<sup>2</sup> (based on a theoretical specific capacity of NMC622 of 200 mAh/g). Subsequently, the In/InLi anode side of the cell was prepared in the same way as for ionic conductivity measurements via DC polarization. The stacked metal foils were placed with In metal adjacent to the argyrodite side of the bilayer SE separator and with Li to the stainless steel electrode.<sup>[48]</sup> Finally, the cell was placed in a homemade stainless-steel holder with an applied pressure of ca. 125 MPa. The cells were cycled at 0.1 C (applied current density of 0.214 mA/cm<sup>2</sup>) in the potential range of 2.6–4.3 V vs. Li/Li<sup>+</sup>, considering that 0 V vs. In/InLi = 0.62 V vs. Li/Li<sup>+</sup>.<sup>[48]</sup>

## Results and Discussion

A schematic description of the one-pot composite preparation approach is presented in Figure S2. The specific synthesis conditions were obtained via trial-and-error optimization of various parameters, such as temperature for water evaporation, annealing temperatures, and precursor mixing conditions. Figure S3 compares the PXRD patterns of Li<sub>3</sub>InCl<sub>6</sub>|CP5% samples prepared with unoptimized conditions to those further used in this study. For the unoptimized sample, one can clearly distinguish the residual presence of precursors as well as multiple side phases. The increased evaporation temperature of 80°C was necessary for synthesizing the composite samples compared to the previously reported 60°C for pure Li<sub>3</sub>InCl<sub>6</sub>.<sup>[29]</sup> The larger volume occupied by the mixed precursors for composite synthesis is due to the additional water required for the redispersion of the CP. Consequently, optimizing the evaporation rate was essential to minimize the processing time, a crucial step for obtaining a clean product.<sup>[44]</sup>

The in-depth investigation of the thermal properties of pristine Li<sub>3</sub>InCl<sub>6</sub> (Figure S4) and CP (Figure S5) in inert and oxygen environments proved the stability of the components during the thermal processing. The presence and stability of the CP in the composites prepared with optimized conditions were evaluated with various complementary methods. Raman spectra show that the addition of the polymer leads to the appearance of the peaks that can be attributed exclusively to the poly(3,4-ethylenedioxythiophene) (PEDOT) and PSS moieties and can be distinguished despite the broad background caused by Li<sub>3</sub>InCl<sub>6</sub> in the range of 900–1600 cm<sup>-1</sup> (Figure 2a, blue trace). Li<sub>3</sub>InCl<sub>6</sub> has various characteristic bands in the range of 100–300 cm<sup>-1</sup>, and a particularly strong one at ca. 290 cm<sup>-1</sup>. Indeed, the latter band is easily distinguished in both the pure Li<sub>3</sub>InCl<sub>6</sub> as well as all the composite samples.<sup>[49,50]</sup> Similarly, the most distinguishable Raman fingerprints of the PEDOT in the composite are the bands appearing at 440, 578, and 988 cm<sup>-1</sup>, characteristic for

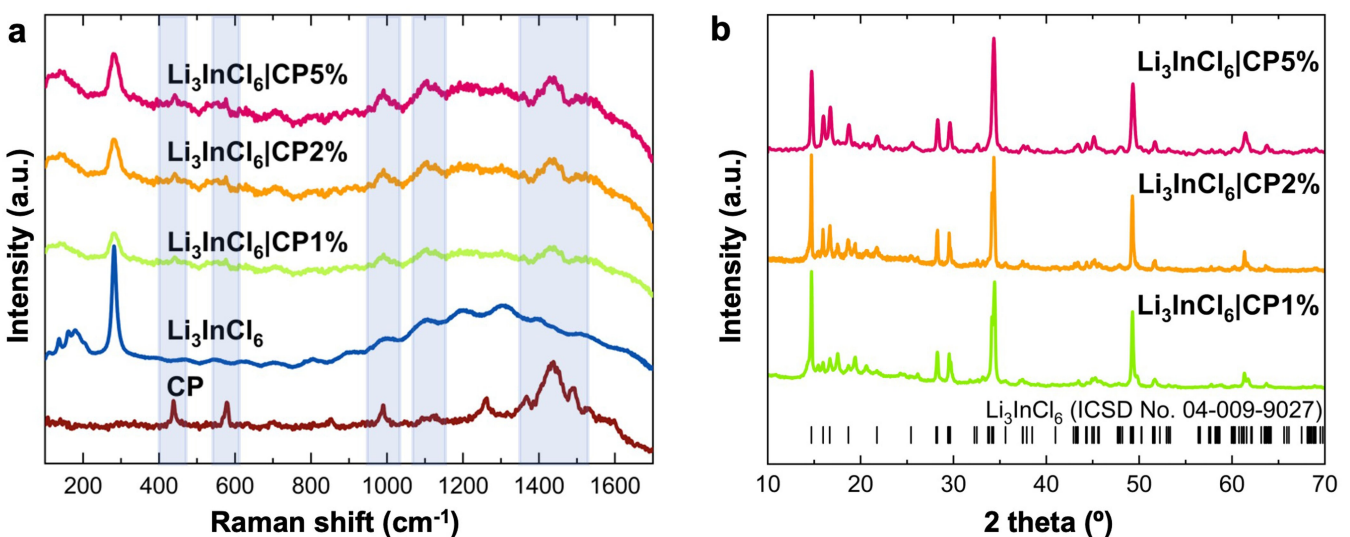


**Figure 2.** (a) Raman spectra of the Li<sub>3</sub>InCl<sub>6</sub>|CPX composites at various wt % of the CP, as-synthesized Li<sub>3</sub>InCl<sub>6</sub> and CP. The shaded regions highlighted in (a) are characteristic bands for the CP component. (b) PXRD patterns of the Li<sub>3</sub>InCl<sub>6</sub>|CPX composites, including reference indices for the target main-Li<sub>3</sub>InCl<sub>6</sub> phase.

oxyethylene ring deformation, as well as the band at  $1445\text{ cm}^{-1}$ , assigned to the symmetric stretching of carbon–carbon double bond.<sup>[51–53]</sup> The signal expected from vibrational modes from PSS moiety is the peak appearing at  $1100\text{ cm}^{-1}$ , which is clearly distinguishable for all composite samples.<sup>[53–56]</sup> Figure S6 shows PXRD pattern of as-synthesized  $\text{Li}_3\text{InCl}_6$  SE, where all reflections align well with the reference pattern for the compound. Additionally, temperature-dependent impedance spectra were analyzed to determine the total ionic conductivity of  $\text{Li}_3\text{InCl}_6$  to  $1.36\text{ mS/cm}$  (Figure S7a, b) and to estimate an activation barrier of  $0.42\text{ eV}$  (Figure S7c). Both values are within the range of those reported by other groups.<sup>[18,28,29,44,57]</sup>

Figure 2b shows the PXRD patterns that confirm a high purity of  $\text{Li}_3\text{InCl}_6$  in the composites at all CP wt%. Small reflections at  $13^\circ$  and  $31^\circ$  were detected for the sample of  $\text{Li}_3\text{InCl}_6|\text{CP}5\%$ . Those reflections were often reported to be found in  $\text{Li}_3\text{InCl}_6$  halide samples obtained both via ball-milling and solution-synthesis.<sup>[18,33,42,44,58,59]</sup> They could be assigned to the presence of the hydrated  $\text{Li}_3\text{InCl}_6$  in very small amounts.<sup>[44,58]</sup>

The TGA of the composites was also performed in open alumina crucibles for samples with different CP loadings (Figure S8). In general, all composites show an initial weight loss of ca. 2–3 wt% at  $90\text{--}150^\circ\text{C}$ , which is assigned to water evaporation. Similar to the  $\text{Li}_3\text{InCl}_6$  (Figure S4), the composites degrade in 2 steps: ca. 60 wt% loss at  $350\text{--}570^\circ\text{C}$  followed by the final decomposition at temperatures above  $650^\circ\text{C}$ . Figure S9 shows exemplary results for the  $\text{Li}_3\text{InCl}_6|\text{CP}5\%$  sample characterized using the modified sample preparation procedure to minimize exposure to ambient air. For such samples, only a

mass change of 0.08 wt% attributable to water evaporation in the range of  $110\text{--}150^\circ\text{C}$  was observed. Results of the DSC for composites with different CP loadings (Figure S10) exclude any phase transitions in the temperature range used for the synthesis of the composites.

SEM images show that the  $\text{Li}_3\text{InCl}_6$  particles in the composites, incl.  $\text{Li}_3\text{InCl}_6|\text{CP}5\%$  (Figure S11), retain sizes comparable to the pristine as-synthesized  $\text{Li}_3\text{InCl}_6$  (Figure S12a–b), while EDX mappings of powder particles (Figure 3a) show a homogenous distribution of In, Cl, sulfur (S) (Figure 3c–d) and oxygen (O) (Figure S13). This suggests that the CP (which contains both sulfur and oxygen) is homogeneously distributed in the composite samples. The SEM-EDX results for  $\text{Li}_3\text{InCl}_6|\text{CP}1\%$  and  $\text{Li}_3\text{InCl}_6|\text{CP}2\%$  show similar particle sizes and similar elemental distributions (Figure S14–S15).

A more direct method to probe the distribution of the CP in the composite samples is KPFM. The latter is an extended AFM method that can directly measure both the topography and surface potential of a flat sample. Such samples were prepared by pressing the SE and composite powders at  $374\text{ MPa}$  for 3 minutes. Figure S16 and Figure S17 show the SEM and EDX characterization of such pressed powders was done to confirm the integrity of the samples upon processing prior to further analysis.

For a surface potential measurement by KPFM, an AC potential with a frequency close to the mechanical resonance frequency of the cantilever and a given amplitude was applied to the AFM tip. This AC potential is fixed by an additional external voltage  $U_{\text{DC}}$  which compensates the surface potential

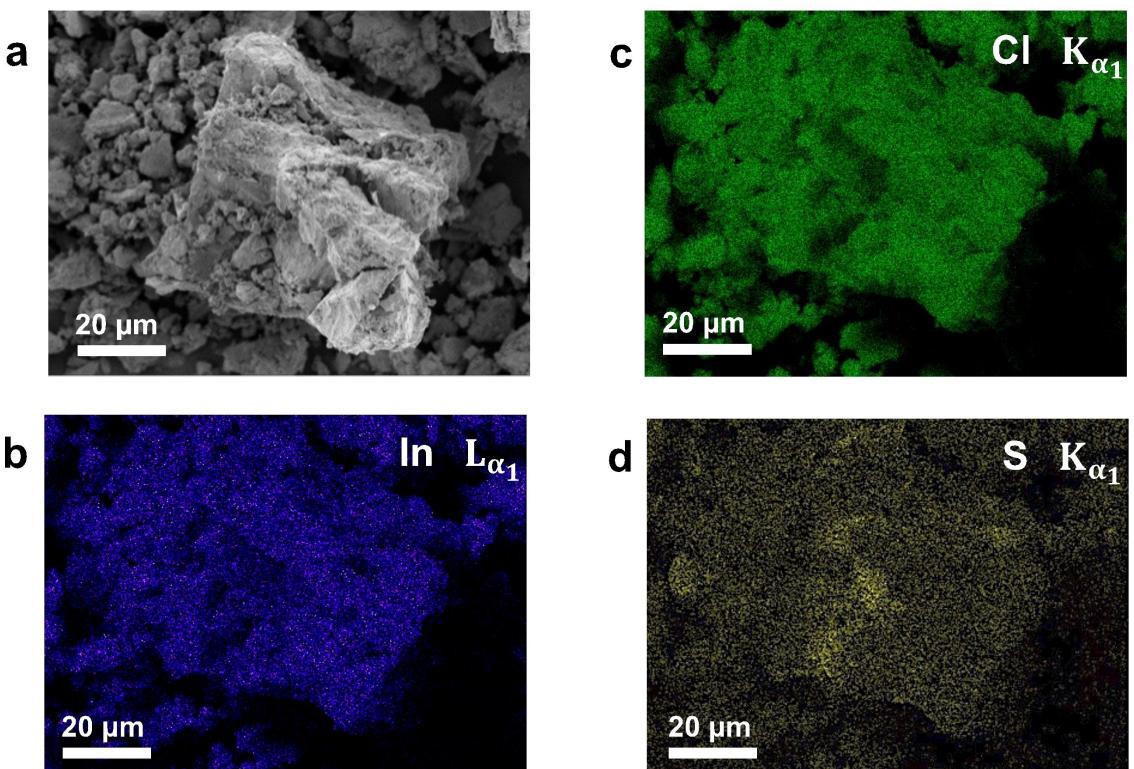


**Figure 3.** (a) SEM of the  $\text{Li}_3\text{InCl}_6|\text{CP}5\%$  powder particle, (b–d) EDX analysis for In, Cl and S from the image in (a).

difference between sample and probe tip according to Equation 1:

$$U_{\text{KPFM}} = -\frac{1}{e} \Delta\varphi_{\text{CPD}} = U_{\text{DC}} \quad (1)$$

A plot of the potential difference  $U_{\text{DC}}$  during the surface scan of the AFM tip yields the KPFM map.<sup>[60,61]</sup> The value in the KPFM images is the contact potential difference ( $\Delta\varphi_{\text{CPD}}$ ) between the AFM tip coated with titanium/iridium (Ti/Ir) and the sample. The working hypothesis here is that the absolute value of the contact potential difference ( $\Delta\varphi_{\text{CPD}}$ ) between the electronically conductive polymer and the Ti/Ir tip should be smaller than that of the  $\Delta\varphi_{\text{CPD}}$  between the SE particles and the tip. As the measured potentials are all negative, areas that are covered in a thicker layer of polymer should show up as lighter areas in the image.

In Figure 4 we compare the topography, surface potential and phase angle images for a pristine  $\text{Li}_3\text{InCl}_6$  and the  $\text{Li}_3\text{InCl}_6|\text{CP}5\%$  composite samples. A grain size analysis of topographic images of  $\text{Li}_3\text{InCl}_6$  (204 grains from 3 images) and  $\text{Li}_3\text{InCl}_6|\text{CP}5\%$  (226 grains from 3 images) results in a grain size of  $164 \text{ nm} \pm 55 \text{ nm}$  and  $110 \text{ nm} \pm 50 \text{ nm}$ , respectively. Based on this, we can conclude that there is no significant difference in the grain sizes of the LIC in the pristine and composite samples. This result is in accordance with the fact that we do not observe significant particle size differences in the SEM images between the two samples. Considering recent reports investigating the role of SE particle size on SSB performance, it is helpful for our study the pristine LIC and composite samples contain similarly sized particles.<sup>[62]</sup> In the case of the surface potential images we see more drastic differences between the two samples. The

image for the pristine sample is in most cases heavily blurred and stripy (Figure 4b), which normally is a sign of electrostatic charging effects often observed for samples with low electronic conductivities. Since  $\text{Li}_3\text{InCl}_6$  is a SE with reported electronic conductivities in the range of  $10^{-9}\text{--}10^{-10} \text{ S/m}$ , this is an expected result.<sup>[18,28,29]</sup> We confirmed such poor electronic conductivities for the as-synthesized  $\text{Li}_3\text{InCl}_6$ , and we calculated a value of  $2\cdot10^{-9} \text{ S/m}$  from DC polarization measurements shown in Figure S18. For the  $\text{Li}_3\text{InCl}_6|\text{CP}5\%$  composite sample we can identify increased (less negative) surface potentials at the edges and in the boundaries between adjacent grains (Figure 4e). Since the net variation in surface potential for the composite samples is small (<50 mV), e.g. the difference between the grain boundaries and grain interior of undoped garnet-type lithium lanthanum zirconate ( $\text{Li}_2\text{La}_3\text{Zr}_2\text{O}_{12}$ ) is in the range of 400 mV, it is important to consider the topography and phase angle images to make correct assignments in the surface potential.<sup>[63]</sup> In Figure 4f we observe specific regions (marked with arrows) where the grain boundaries show a higher phase contrast (lighter coloring) than the grains, which is generally associated with an increased elasticity and/or adhesion compared to the surrounding. In this region, we also observe minor topography changes (only a few nm, Figure 4d) and the surface potential shows some measurable differences/structure (Figure 4e).

A direct comparison of the surface potential images shows that the pristine  $\text{Li}_3\text{InCl}_6$  sample has an overall lower (more negative) potential than the  $\text{Li}_3\text{InCl}_6|\text{CP}5\%$  composite, which serves as definite evidence of the incorporation of the conductive polymer and its effect on its electrical properties. The fact that differences in the phase image of the composite sample (Figure 4f) are in a similar range to the pristine  $\text{Li}_3\text{InCl}_6$

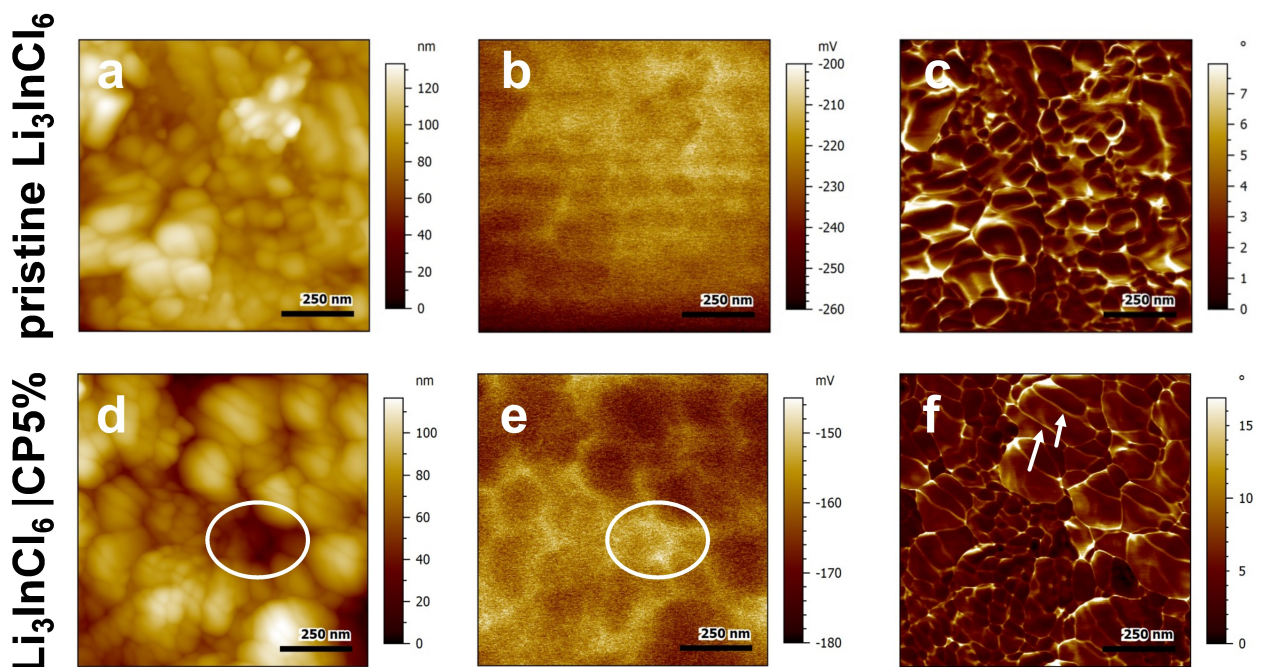


**Figure 4.** Exemplary topography (a and d), surface potential (b and e) and phase (c and f) images for the pristine  $\text{Li}_3\text{InCl}_6$  sample (upper row) and the  $\text{Li}_3\text{InCl}_6|\text{CP}5\%$  composite samples (bottom row).

sample (Figure 4c) also indicates that the addition of the conductive polymer binder does not significantly change the (local) elasticity of the composite sample for the analyzed  $\text{Li}_3\text{InCl}_6|\text{CP}5\%$ . Note that greater surface potential differences are also observed in other regions of the probed area (marked with circles in Figure 4e). However, the circled area also corresponds to grain edges with large topographical differences and are therefore interpreted as artifacts. Despite this, it is reasonable to interpret these results such that the CP is located at the surface/grain boundaries between  $\text{Li}_3\text{InCl}_6$  particles in the composite sample.

The final step was to evaluate the (bulk) electrochemical properties of such composites when used as a catholyte component for NMC-based solid-state cells. Firstly, we determined the partial electronic and ionic conductivities of the samples via DC polarization (Figure 5a). The obtained results correspond well to the values reported earlier for similar pristine systems.<sup>[62,64,65]</sup> To do this, we mixed the  $\text{Li}_3\text{InCl}_6|\text{CPX}$  composites with NMC622 (30:70 wt%). For the determination of the

partial electronic conductivity, mixed cathode composites were subsequently pressed as pellets. SEM and EDX results suggest that both the  $\text{Li}_3\text{InCl}_6|\text{CP}5\%$  composite and the NMC622 remain unharmed during processing (Figure S19). We observe that the partial electronic conductivity of the cathode composite increases four-fold upon the incorporation of 1 wt% of CP in the cathode composite in comparison to just  $\text{Li}_3\text{InCl}_6$  combined directly with NMC622. Moreover, upon further increasing the CP content, we measure a monotonic increase in the partial electronic conductivity of the cathode composites. For the partial ionic conductivity measurements, symmetric electron-blocking cells were assembled with a solid-electrolyte separator and In/InLi on both sides of the cathode composite. The results of partial ionic conductivity suggest the monotonous decrease of the effective ionic conductivity with the increase of the CP content. The decrease in the measured ionic conductivity can be attributed to the more significant blockage of the ion pathways at higher loadings of CP hindering the ion transport. Since a significant mismatch in effective ionic and

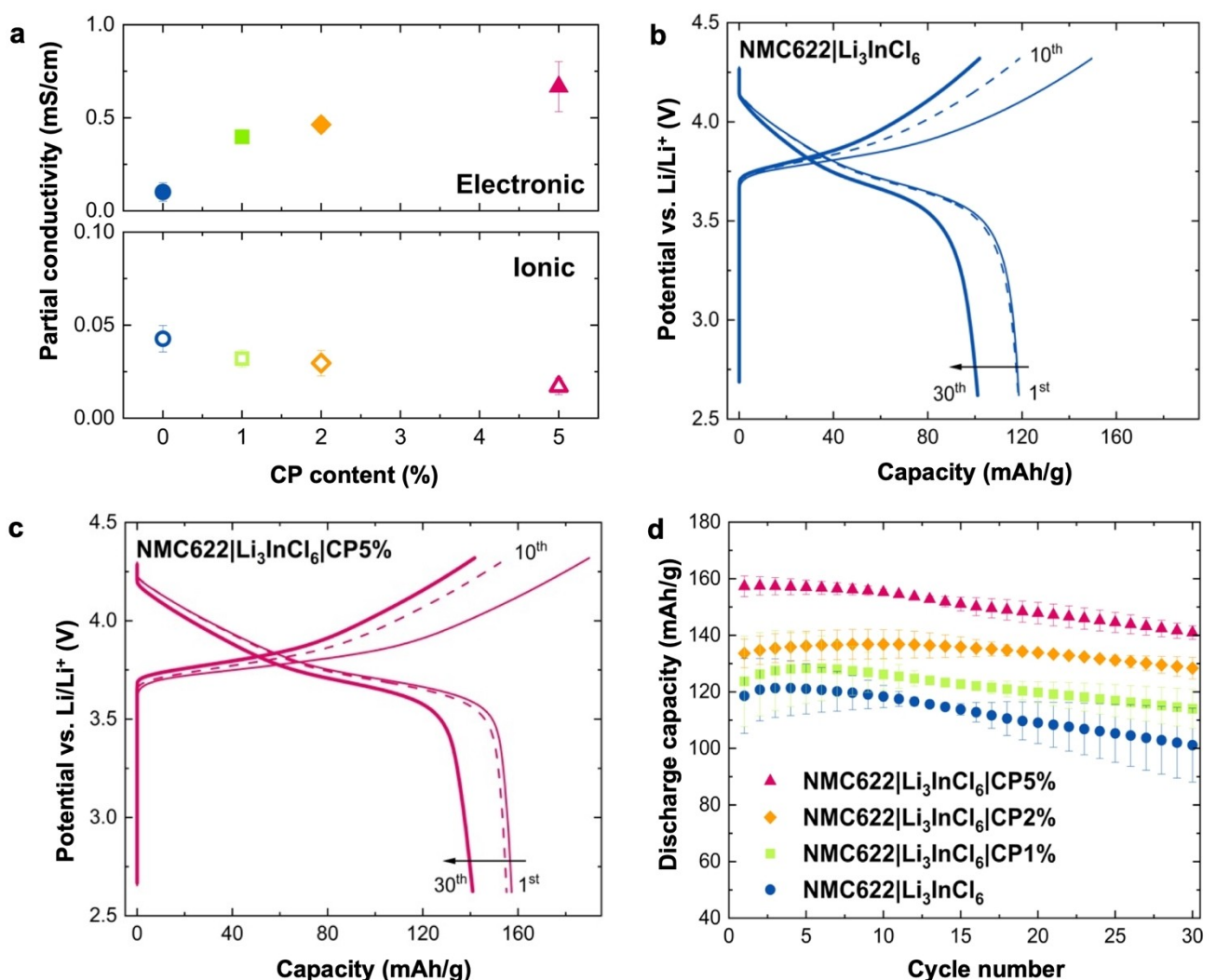


**Figure 5.** Evaluation of electrochemical performance of the composites. (a) Partial electronic (top) and ionic (bottom) conductivities measured via DC polarization, (b and c) charge-discharge curves of the cells (b) without and (c) with CP (5 wt% to  $\text{Li}_3\text{InCl}_6$ ) in the catholyte composite, (d) discharge capacities up to 30 cycles for cells with different catholyte composites at 0.1 C.

electronic conductivities was observed for the investigated CP loadings (0–5 wt.%), further increasing CP loading was not pursued in this research. Moreover, earlier research has also highlighted that a higher amount of conductive additive can lead to accelerated degradation of the halide-solid electrolytes in the composite.<sup>[18–21]</sup>

Such cathode composites were then integrated into solid-state (half-)cells. Due to the well-known instability of the halide SE against Li metal, we tested these cathode composites in cells that used a bilayer separator with  $\text{Li}_3\text{InCl}_6$  and  $\text{Li}_6\text{PS}_5\text{Cl}$  layers against In/Liln as an anode.<sup>[66,67]</sup> Moreover, in this configuration we can truly focus on the effect of the cathode additives, namely the  $\text{Li}_3\text{InCl}_6$  | CPX composites, on the performance of the cells. Figure 5b shows exemplary charge-discharge curves for the NMC622 |  $\text{Li}_3\text{InCl}_6$  catholyte, with an initial discharge capacity of 120 mAh/g that decays over the course of 30 cycles to ca. 100 mAh/g. The cathode composite with the highest CP content in this study (5 wt%) shows initial discharge capacities of almost 160 mAh/g. The charge-discharge curves for the other two composites are compiled in Figures S20. Furthermore, the capacity retention and Coulombic efficiencies of all cells over cycling are summarized in Figure S21 and Figure S22 correspondingly. In Figure 5d we compare the average performance of all cells tested and can confirm a monotonic increase in the initial discharge capacity of the cells with increasing CP content which is in accordance with the increase of the partial electronic conductivity of cathode composite. Interestingly, the cycling stability of the cells does not correlate with the amount of CP in the cathode composite. The cells with better capacity retention are those with 2 wt% of CP, in which a capacity fade of only 4% is observed over the course of 30 cycles, similarly showing highest Coulombic efficiency amounting to 99.6%. Previous reports have demonstrated the instability of  $\text{Li}_3\text{InCl}_6$ -based catholytes that contain carbon additives and a bilayer separator configuration.<sup>[18–20]</sup> However, these weaknesses can be overcome by the implementation of thin oxide-based ionically conducting layers that physically separate the  $\text{Li}_3\text{InCl}_6$  and the thiophosphate-based electrolyte.<sup>[19]</sup> Despite the resulting complexity of the separator heterostructure, the stability of the cells is very promising.

Although a direct comparison of this work with the results reported by other research groups is challenging due to the different cell chemistries and active material loadings, our cycling results are comparable to previous reports in terms of delivered initial capacities.<sup>[18–21,57]</sup> It was recently reported that cathode composites in which the partial ionic and partial electronic conductivities are matched, maximize the specific capacities of sulfide half-cells.<sup>[62,64,68]</sup> Similarly we observe a direct correlation between the CP content in the cathode composite and the initial discharge capacity of all cells (Figure 6). However, the capacity retention of the cells after 30 cycles does not show a similar correlation. This is related to the fact that upon incorporating a new component in the catholyte (in this case the CP), we must re-optimize the volume fractions of the solid electrolyte and the cathode active material. Since it is difficult to assess the volume occupied by the CP at such low content in these composites, the parameter space to explore

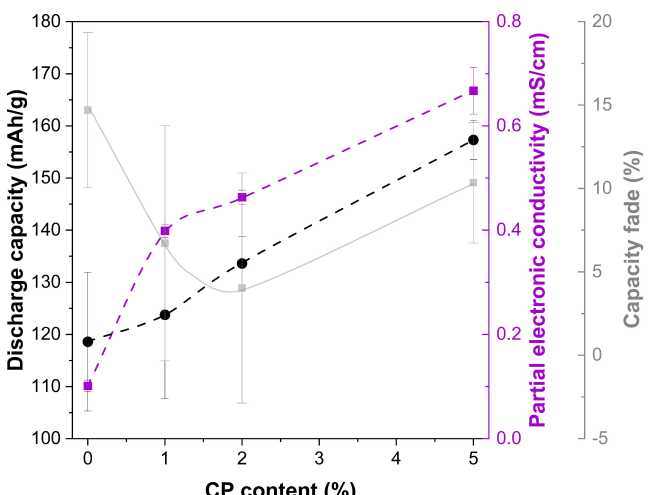


Figure 6. Correlation between the initial discharge capacities of cells, the effective electronic conductivities of the cathode composites and the capacity fade after 30 cycles at 0.1 C on the CP content.

and find the optimum is very large and outside of the scope of the present work. Moreover, the faster degradation of capacity in samples with higher CP loading can be explained by the fact that the CP occupies more space in the intergranular region between  $\text{Li}_3\text{InCl}_6$  particles, hindering ionic transport due to its lack of ionic conductivity properties (Figure 5a). This impediment is due to the CP taking up more volume in the intergranular space (Figure 4f), which restricts the movement of ions. Nonetheless, efforts to optimize the system are currently underway in our group. Moreover, previous reports have shown that the processing of solid-state materials, e.g., ball-milling versus hand-grinding, can have a strong impact on their electrochemical properties and solid-state battery performance.<sup>[69]</sup> Therefore, the processing method of the cathode composites is another parameter space that can be explored and may result in better-performing cells. Ideally, we can extend our optimized one-pot, water-mediated synthesis to incorporate cathode active materials directly and prepare the catholyte powder in a single, scalable step.<sup>[42]</sup>

## Conclusions

In summary, we report a one-pot water-mediated synthesis of halide solid electrolyte-conductive polymer composites. The synthesis conditions have been optimized such that high-purity  $\text{Li}_3\text{InCl}_6$  is embedded in a well-distributed matrix of PEDOT:PSS, acting both as a binder and electronically conducting additive. The latter claim is supported by the following techniques: PXRD, TA, SEM, Raman, and KPFM. It was shown that the composites remain unharmed even after mixing with NMC622 and pressing in pellets. DC polarization measurements revealed a significant increase in electronic conductivities with higher CP content. Integration in sulfide half-cells showed promising results in the improved initial discharge capacities, signifying that the addition of the CP allowed to address CAM more

efficiently in the cathode composite. These results serve as the foundation of further studies in the development of more efficient, scalable, and greener routes for the preparation of cathode composites for applications in SSBs.

## Supporting Information

Chemical structure of PEDOT:PSS, schematic for the preparation of the  $\text{Li}_3\text{InCl}_6|\text{CP}$  composites, additional PXRD results for composites prepared under unoptimized conditions, TGA and DSC traces for additional samples, PXRD of SE, T-dependent EIS of SE, additional SEM and EDX images for as-prepared and pressed powders, DC polarization data, additional charge-discharge curves, capacity retentions and Coulombic efficiencies for all cells.

## Acknowledgements

This work was funded by the Ministry of Culture and Science of the State North Rhine-Westphalia as part of the International Graduate School BACCARA. We are grateful to Münster Electrochemical Energy Technology (MEET), the Center for Nanotechnology (CeNTech) and the Zeier Research Group at the University of Münster for access to lab facilities. Dr. Michael R. Nellist is acknowledged for support at the initial stages of this project. Special thanks are offered to Debbie Berghus who performed the DSC and TGA measurements. N.M.V-B. gratefully acknowledges the support of the Helmholtz Association via the Young Investigator Group Program. Open Access funding enabled and organized by Projekt DEAL.

## Conflict of Interests

The authors declare no conflict of interest.

## Data Availability Statement

The data that support the findings of this study are available from the corresponding author upon reasonable request.

**Keywords:** composite materials · solid-state catholytes · halide solid electrolytes · aqueous cathode processing •

- [1] A. Masias, J. Marcicki, W. A. Paxton, *ACS Energy Lett.* **2021**, *6*, 621–630.
- [2] A. M. Bates, Y. Preger, L. Torres-Castro, K. L. Harrison, S. J. Harris, J. Hewson, *Joule* **2022**, *6*, 742–755.
- [3] J. Janek, W. G. Zeier, *Nat. Energy* **2016**, *1*, 16141.
- [4] T. Famprikis, P. Canepa, J. A. Dawson, M. S. Islam, C. Masquelier, *Nat. Mater.* **2019**, *18*, 1278–1291.
- [5] T. Krauskopf, F. H. Richter, W. G. Zeier, J. Janek, *Chem. Rev.* **2020**, *120*, 7745–7794.
- [6] X. B. Cheng, C. Z. Zhao, Y. X. Yao, H. Liu, Q. Zhang, *Chem* **2019**, *5*, 74–96.
- [7] K. J. Kim, M. Balaish, M. Wadaguchi, L. Kong, J. L. M. Rupp, *Adv. Energy Mater.* **2021**, *11*, 2002689.
- [8] T. Shi, Y. Q. Zhang, Q. Tu, Y. Wang, M. C. Scott, G. Ceder, *J. Mater. Chem. A* **2020**, *8*, 17399–17404.
- [9] P. Minnmann, F. Strauss, A. Bielefeld, R. Ruess, P. Adelhelm, S. Burkhardt, S. L. Dreyer, E. Trevisanello, H. Ehrenberg, T. Brezesinski, F. H. Richter, J. Janek, *Adv. Energy Mater.* **2022**, *12*, 2201425.
- [10] J. Zhang, Z. Chen, Q. Ai, T. Terlier, F. Hao, Y. Liang, H. Guo, J. Lou, Y. Yao, *Joule* **2021**, *5*, 1845–1859.
- [11] X. Miao, S. Guan, C. Ma, L. Li, C. W. Nan, *Adv. Mater.* **2023**, *35*, 2206402, <https://doi.org/10.1002/adma.202206402>.
- [12] C. Wang, X. Sun, *Engineering* **2023**, *21*, 32–35.
- [13] Y. Xiao, Y. Wang, S. H. Bo, J. C. Kim, L. J. Miara, G. Ceder, *Nat. Rev. Mater.* **2020**, *5*, 105–126.
- [14] S. Sen, E. Trevisanello, E. Niemöller, B. X. Shi, F. J. Simon, F. H. Richter, J. Mater. Chem. A **2021**, *9*, 18701–18732.
- [15] M. J. Wang, E. Kazyak, N. P. Dasgupta, J. Sakamoto, *Joule* **2021**, *5*, 1371–1390.
- [16] L. Z. Fan, H. He, C. W. Nan, *Nat. Rev. Mater.* **2021**, *6*, 1003–1019.
- [17] K. Wang, Q. Ye, J. Zhang, H. Huang, Y. Gan, X. He, W. Zhang, *Front. Mater.* **2021**, *8*, 727617.
- [18] T. Koç, F. Marchini, G. Rousse, R. Dugas, J. M. Tarascon, *ACS Appl. Energ. Mater.* **2021**, *4*, 13575–13585.
- [19] T. Koç, M. Hallot, E. Quemin, B. Hennequart, R. Dugas, A. M. Abakumov, C. Lethien, J. M. Tarascon, *ACS Energy Lett.* **2022**, *7*, 2979–2987.
- [20] S. Deng, M. Jiang, N. Chen, W. Li, M. Zheng, W. Chen, R. Li, H. Huang, J. Wang, C. V. Singh, X. Sun, *Adv. Funct. Mater.* **2022**, *32*.
- [21] H. Kwak, S. Wang, J. Park, Y. Liu, K. T. Kim, Y. Choi, Y. Mo, Y. S. Jung, *ACS Energy Lett.* **2022**, *7*, 1776–1805.
- [22] L. Peng, C. Yu, Z. Zhang, H. Ren, J. Zhang, Z. He, M. Yu, L. Zhang, S. Cheng, J. Xie, *Chemical Engineering Journal* **2022**, *430* (2), 132896, <https://doi.org/10.1016/j.cej.2021.132896>.
- [23] S. Ohno, C. Rosenbach, G. F. Dewald, J. Janek, W. G. Zeier, *Adv. Funct. Mater.* **2021**, *31*, 2010620, <https://doi.org/10.1002/adfm.202010620>.
- [24] D. H. S. Tan, E. A. Wu, H. Nguyen, Z. Chen, M. A. T. Marple, J. M. Doux, X. Wang, H. Yang, A. Banerjee, Y. S. Meng, *ACS Energy Lett.* **2019**, *4* (10), 2418–2427, <https://doi.org/10.1021/acsenergylett.9b01693>.
- [25] F. Walther, S. Randau, Y. Schneider, J. Sann, M. Rohnke, F. H. Richter, W. G. Zeier, J. Janek, *Chem. Mater.* **2020**, *32*, 6123–6136.
- [26] W. Zhang, T. Leichtweiß, S. P. Culver, R. Koever, D. Das, D. A. Weber, W. G. Zeier, J. Janek, *ACS Appl. Mater. Interfaces* **2017**, *9*, 35888–35896.
- [27] D. Park, H. Park, Y. Lee, S. O. Kim, H. G. Jung, K. Y. Chung, J. H. Shim, S. Yu, *ACS Appl. Mater. Interfaces* **2020**, *12*, 34806–34814.
- [28] X. Li, J. Liang, J. Luo, M. Norouzi Banis, C. Wang, W. Li, S. Deng, C. Yu, F. Zhao, Y. Hu, T. K. Sham, L. Zhang, S. Zhao, S. Lu, H. Huang, R. Li, K. R. Adair, X. Sun, *Energy Environ. Sci.* **2019**, *12*, 2665–2671.
- [29] X. Li, J. Liang, N. Chen, J. Luo, K. R. Adair, C. Wang, M. N. Banis, T. Sham, L. Zhang, S. Zhao, S. Lu, H. Huang, R. Li, X. Sun, *Angew. Chem.* **2019**, *58*, 16427–16432.
- [30] X. Luo, D. Cai, X. Wang, X. Xia, C. Gu, J. Tu, *ACS Appl. Mater. Interfaces* **2022**, *14*, 29844–29855.
- [31] X. Nie, J. Hu, C. Li, *Interdisciplinary Materials* **2023**, *2*, 365–389.
- [32] J. Liang, X. Li, K. R. Adair, X. Sun, *Acc. Chem. Res.* **2021**, *54*, 1023–1033.
- [33] P. Molaiyan, S. E. Mailhiot, K. Voges, A. M. Kantola, T. Hu, P. Michalowski, A. Kwade, V. V. Telkki, U. Lassi, *Mater Des* **2023**, *227*, 111690, <https://doi.org/10.1016/j.matdes.2023.111690>.
- [34] K. Wang, Q. Ye, J. Zhang, H. Huang, Y. Gan, X. He, W. Zhang, *Front Mater.* **2021**, *8*, 727617, <https://doi.org/10.3389/fmats.2021.727617>.
- [35] S. Y. Kim, H. Cha, R. Kostecki, G. Chen, *ACS Energy Lett.* **2023**, *8*, 521–528.
- [36] B. Zhao, Y. Lu, B. Yuan, Z. Wang, X. Han, *Mater. Lett.* **2022**, *310*.
- [37] W. Kim, J. Noh, S. Lee, K. Yoon, S. Han, S. Yu, K. H. Ko, K. Kang, *Advanced Materials* **2023**, *35*, 2301631, <https://doi.org/10.1002/adma.202301631>.
- [38] C. Zhao, J. Liang, X. Li, N. Holmes, C. Wang, J. Wang, F. Zhao, S. Li, Q. Sun, X. Yang, J. Liang, X. Lin, W. Li, R. Li, S. Zhao, H. Huang, L. Zhang, S. Lu, X. Sun, *Nano Energy* **2020**, *75*, 105036, <https://doi.org/10.1016/j.nanoen.2020.105036>.
- [39] C. Li, L. Gu, J. Maier, *Adv. Funct. Mater.* **2012**, *22*, 1145–1149.
- [40] J. Hu, K. Chen, C. Li, *ACS Appl. Mater. Interfaces* **2018**, *10*, 34322–34331.
- [41] M. Lei, X. Wu, Y. Liu, K. Chen, J. Hu, C. Li, *Nano Res.* **2023**, *16*, 8469–8477.
- [42] C. Wang, J. Liang, M. Jiang, X. Li, S. Mukherjee, K. Adair, M. Zheng, Y. Zhao, F. Zhao, S. Zhang, R. Li, H. Huang, S. Zhao, L. Zhang, S. Lu, C. V. Singh, X. Sun, *Nano Energy* **2020**, *76*, 105015.
- [43] S. P. Culver, R. Koever, W. G. Zeier, J. Janek, *Adv. Energy Mater.* **2019**, *9*, 1900626.
- [44] R. L. Sacci, T. H. Bennett, A. R. Drews, V. Anandan, M. J. Kirkham, L. L. Daemen, J. Nanda, *J. Mater. Chem. A* **2021**, *9*, 990–996.

- [45] H. W. Liu, C. C. Lin, P. Y. Chang, S. C. Haw, H. S. Sheu, J. M. Chen, C. C. Chen, R. J. Jeng, N. L. Wu, *J. Solid State Electrochem.* **2022**, *26*, 2089–2096.
- [46] C. Örnek, C. Leygraf, J. Pan, *Corros. Eng. Sci. Technol.* **2019**, *54*, 185–198.
- [47] W. Zhang, D. A. Weber, H. Weigand, T. Arlt, I. Manke, D. Schröder, R. Koerver, T. Leichtweiss, P. Hartmann, W. G. Zeier, J. Janek, *ACS Appl. Mater. Interfaces* **2017**, *9*, 17835–17845.
- [48] A. L. Santhosha, L. Medenbach, J. R. Buchheim, P. Adelhelm, *Batteries & Supercaps* **2019**, *2*, 524–529.
- [49] S. Wang, X. Xu, C. Cui, C. Zeng, J. Liang, J. Fu, R. Zhang, T. Zhai, H. Li, *Adv. Funct. Mater.* **2022**, *32*, 2108805.
- [50] W. Li, J. Liang, M. Li, K. R. Adair, X. Li, Y. Hu, Q. Xiao, R. Feng, R. Li, L. Zhang, S. Lu, H. Huang, S. Zhao, T. K. Sham, X. Sun, *Chem. Mater.* **2020**, *32*, 7019–7027.
- [51] W. Shi, Q. Yao, S. Qu, H. Chen, T. Zhang, L. Chen, *NPG Asia Mater.* **2017**, *9*, e405.
- [52] W. W. Chiu, J. Travas-Šejdić, R. P. Cooney, G. A. Bowmaker, *J. Raman Spectrosc.* **2006**, *37*, 1354–1361.
- [53] S. H. Chang, C. H. Chiang, F. S. Kao, C. L. Tien, C. G. Wu, *IEEE Photonics J* **2014**, *6*, 8400307.
- [54] D. Antiohos, G. Folkes, P. Sherrell, S. Ashraf, G. G. Wallace, P. Aitchison, A. T. Harris, J. Chen, A. I. Minett, *J. Mater. Chem.* **2011**, *21*, 15987–15994.
- [55] Y.-K. Han, M.-Y. Chang, W.-Y. Huang, H.-Y. Pan, K.-S. Ho, T.-H. Hsieh, S.-Y. Pan, *J. Electrochem. Soc.* **2011**, *158*, K88–K93.
- [56] R. Chen, K. Sun, Q. Zhang, Y. Zhou, M. Li, Y. Sun, Z. Wu, Y. Wu, X. Li, J. Xi, C. Ma, Y. Zhang, J. Ouyang, *iScience* **2019**, *12*, 66–75.
- [57] I. Kochetkov, T. T. Zuo, R. Ruess, B. Singh, L. Zhou, K. Kaup, J. Janek, L. Nazar, *Energy Environ. Sci.* **2022**, *15*, 3933–3944.
- [58] K. Wang, Q. Ren, Z. Gu, C. Duan, J. Wang, F. Zhu, Y. Fu, J. Hao, J. Zhu, L. He, C. W. Wang, Y. Lu, J. Ma, C. Ma, *Nat. Commun.* **2021**, *12*, 4410.
- [59] B. Helm, R. Schlem, B. Wankmiller, A. Banik, A. Gautam, J. Ruhl, C. Li, M. R. Hansen, W. G. Zeier, *Chem. Mater.* **2021**, *33*, 4773–4782.
- [60] M. Salerno, S. Dante, *Materials* **2018**, *11*, 951.
- [61] W. Melitz, J. Shen, A. C. Kummel, S. Lee, *Surf. Sci. Rep.* **2011**, *66*, 1–27.
- [62] E. Schlaутmann, A. Weiß, O. Maus, L. Ketter, M. Rana, S. Puls, V. Nickel, C. Gabby, C. Hartnig, A. Bielefeld, W. G. Zeier, *Adv Energy Mater* **2023**, *13*, 2302309, <https://doi.org/10.1002/aenm.202302309>.
- [63] Y. Zhu, S. Wu, Y. Pan, X. Zhang, Z. Yan, Y. Xiang, *Nanoscale Res. Lett.* **2020**, *15*, 153.
- [64] T. A. Hendriks, M. A. Lange, E. M. Kiens, C. Baeumer, W. G. Zeier, *Batteries & Supercaps* **2023**, *6*.
- [65] G. F. Dewald, S. Ohno, J. G. C. Hering, J. Janek, W. G. Zeier, *Batteries & Supercaps* **2021**, *4*, 183–194.
- [66] L. M. Rieger, R. Schlem, J. Sann, W. G. Zeier, J. Janek, *Angew. Chem. Int. Ed.* **2021**, *60*, 6718–6723.
- [67] C. Wang, J. Liang, J. T. Kim, X. Sun, *Sci. Adv.* **2022**, *8*, eadc9516.
- [68] P. Minnmann, L. Quillman, S. Burkhardt, F. H. Richter, J. Janek, *J. Electrochem. Soc.* **2021**, *168*, 040537.
- [69] S. Ohno, R. Koerver, G. Dewald, C. Rosenbach, P. Titscher, D. Steckermeier, A. Kwade, J. Janek, W. G. Zeier, *Chem. Mater.* **2019**, *31*, 2930–2940.

Manuscript received: September 27, 2023

Revised manuscript received: December 6, 2023

Accepted manuscript online: December 28, 2023

Version of record online: January 15, 2024